Mater Eng Res, 2023, 5(1): 256-264
DOI: 10.25082/MER.2023.01.002

RESEARCH ARTICLE

# Load-induced local phase transformation and modulus of shape memory alloys under spherical indentation by finite element method

**Sayed Ehsan Saghaian**[1*] **Y. C. Lu**[2] **Sayed M. Saghaian**[3] **Haluk E. Karaca**[2]

[1] Mechanical and Civil Engineering, Florida Institute of Technology, Melbourne, FL 32901, USA
[2] Department of Mechanical Engineering, University of Kentucky, Lexington, KY 40506, USA
[3] Department of Mechanical and Aerospace Engineering, Illinois Institute of Technology, Chicago, IL 60616, USA



**Correspondence to:** Sayed Ehsan Saghaian, Mechanical and Civil Engineering, Florida Institute of Technology, Melbourne, FL 32901, USA;
Email: ssaghaian@fit.edu

**Received:** April 13, 2023;
**Accepted:** June 9, 2023;
**Published:** June 14, 2023.

**Citation:** Saghaian SE, Lu YC, Saghaian SM, *et al.* Load-induced local phase transformation and modulus of shape memory alloys under spherical indentation by finite element method. *Mater Eng Ress*, 2023, **5**(1): 256-264. https://doi.org/10.25082/MER.2023.01.002



**Abstract:** Shape memory alloys are a unique class of materials that are capable of large reversible deformations under external stimuli such as stress or temperature. The present study examines the phase transformations and mechanical responses of NiTi and NiTiHf shape memory alloys under the loading of a spherical indenter by using a finite element model. It is found that the indentation unloading curves exhibit distinct changes in slopes due to the reversible phase transformations in the SMAs. The normalized contact stiffness ($F/S^2$) of the SMAs varies with the indentation load (depth) as opposed to being constant for conventional single-phase materials. The load-induced phase transformation that occurred under the spherical indenter was simulated numerically. It is observed that the phase transformation phenomenon in the SMA induced by an indentation load is distinctly different from that induced by a uniaxial load. A pointed indenter produces a localized deformation, resulting in a stress (load) gradient in the specimen. As a result, the transformation of phases in SMAs induced by an indenter can only be partially completed. The overall modulus of the SMAs varies continuously with the indentation load (depth) as the average volumetric fraction of the martensite phase varies. For NiTi ($E_a > E_m$), the modulus decreases with the depth, while for NiTiHf ($E_a < E_m$), the modulus increases with the depth. The predicted young modules during indentation modeling agree well with experimental results. Finally, the phase transformation of the SMAs under the indenter is not affected by the post-yield behavior of the materials.

**Keywords:** shape memory alloys, nanoindentation, spherical indenter, phase transformation, finite element method

## 1 Introduction

Nanoindentation has become the standard method for studying the mechanics and deformation of materials at small scales. In this test, an indenter tip is pushed into the surface of the material under precise load or displacement control (the load and displacement resolutions are typically in the magnitudes of micro-Newton ($\mu$N) and nanometer (nm), respectively). The extremely small loads and displacements can be recorded continuously throughout the loading-unloading cycle, resulting in the quantitative indentation load-depth responses from which the properties of the material may be extrapolated [1, 2]. The indenter can be of various shapes, including a three-faced pyramid (Berkvoich), sphere, cone, and flat. The proper selection of indenter geometry allows for examining various mechanical deformation modes in the materials, such as elastic, elastic-plastic, visco-elastic, fracture, and fatigue. So far, nanoindentation has been successfully used for testing various single-phase materials (metals, ceramics, polymers, thin films, and advanced materials, including nanomaterials) [1–9].

Shape memory alloys (SMAs) are a unique class of metal alloys capable of reversible phase transformations under external stimuli. The solid-to-solid phase transformation in an SMA involves the ordered motion of the atoms in their crystal structure in a way that the structure transforms from one lattice type to another. Nickel-Titanium (*i.e.*, NiTi or Nitinol) is the most common shape memory alloy (SMA) that demonstrates stable shape-memory effect and superelasticity behaviors and has excellent erosion, corrosion and wear resistance, and good biocompatibility [10–15]. In NiTi, the austenite phase is a highly symmetric, cubic crystal structure, while the martensite is monoclinic [16, 17]. Due to the microstructural differences, these two phases exhibit different properties (e.g., elastic modulus, strength, and ductility). There is a growing interest in probing the mechanical properties and deformation of SMAs using the nanoindentation technique since these alloys have been increasingly used as micro-surgery devices, thin films, MEMS, etc. [16–22]. However, compared to conventional materials

(*i.e.*, single phase materials), the indentation responses of SMAs are more complicated due to the phase transformation and shape memory effect (SME). In a broad sense, an SMA may be considered a composite that is consisted of two phases: austenite and martensite. The volume fractions of these phases are not fixed and highly depend on the stress, which would continuously alter during the loading/unloading of the indenter. Furthermore, martensite can be in self-accommodating or reoriented forms under the applied load from an indenter.

Nanoindentation experiments have been reported to study the mechanical responses of various shape memory alloys, mainly by examining the shape memory behaviors [23–25]. The high performance of superelasticity with the large recoverable depth on NiTi alloys has been reported [24]. Additionally, a novel technique of using Vickers indenter to induce a two-way shape memory effect (TWSME) on a NiTi alloy has been proposed [25, 26]. It is observed that spherical indent in austenite NiTi specimen can fully recover upon unloading, while indent in martensite can only partially recover. Numerical simulations on the nanoindentation of SMAs have also been performed [27–29]. The studies are mainly focused on the phenomenological aspects of the indentation, *i.e.*, the variations of contact depth, contact width, hardness, etc. It has been suggested that the nanoindentation technique may be used to extract the material properties of the SMA constituents (austenite modulus ($E_a$) and the martensite modulus ($E_m$)) [29]. However, the analysis was only tested on one individual SMA that has a higher austenite modulus ($E_a/E_m > 1$). In addition, most simulations have assumed that the SMAs exhibit elastic deformation only, and the effects of plastic deformation have been ignored.

Therefore, the present work examines the elastic-plastic indentation behaviors of two distinct SMAs using a finite element model for spherical indenters. The advantage of using a blunt indenter (spherical or flat-ended indenter) is that an indenter of such shape can induce large loads beneath the indenter surface, which allows for the study of stress- induced phase transformation in the SMAs. The other advantage of using a spherical indenter (in comparison with sharp indenters) is that the indentation strain can be directly associated with the uniaxial strain through the well-known Tabor's relation [30]. The materials studied are NiTi and NiTiHf SMAs that exhibit distinct elastic properties [29, 31]. NiTi is one of the most commonly used SMAs that typically exhibit low transformation temperatures and strength and has been employed in various applications such as aerospace, automotive, medical, and oil industries [32–35]. However, with the addition of a ternary element Hf (partially replacing Ti content), the NiTiHf alloys present higher transformation temperatures and strength [36,37]. Thus this alloy is functional at elevated temperatures and harsh environments and is currently moving to commercial production.

# 2 Numerical procedures

## 2.1 Finite element model for spherical indentation

The indentation behavior of SMAs under a spherical indenter was studied by the finite element method using commercial software ABAQUS [38]. Due to the symmetries of both geometry and loading conditions, the spherical indentation problem can be reduced to a two-dimensional, axisymmetric model (Figure 1). Since the indenter was much stiffer than the SMAs, the indenter was considered to be perfectly rigid and modeled as a rigid analytical surface. The size (radius, R) of the indenter was 50 $\mu$m. Four-node, axisymmetric, linear, quadrilateral elements, CAX4R, were used to model the SMA solids. The overall size of the finite element model was large enough to ensure the characteristic of a half space. The finer mesh was created around the indenter tip to ensure accurate modeling of the contact between the sample and the indenter. A frictionless contact was assumed at the interface of the indenter and specimen.

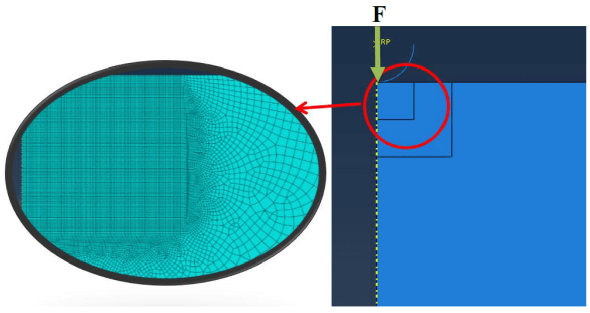


**Figure 1** The geometry and mesh utilized in the finite element model for the indentation of SMAs by a spherical indenter

As shown in Figure 1, a rigid, spherical indenter is pressed onto the surface of a semi-infinite

SMA specimen. The contact boundary conditions in a cylindrical coordinate ($\alpha$, $\theta$, z) are

$$\sigma_{rz}(r,0) = 0 \quad \text{for } r < a \tag{1a}$$

$$\sigma_{rz}(r,0) = \sigma_{zz}(r,0) = 0 \quad \text{for } r > a \tag{1b}$$

$$u_z(r,0) = f(r) - h \quad \text{for } r < a \tag{1c}$$

where $\sigma_{rz}$ and $\sigma_{zz}$ are respectively the shear and normal components of the stress tensor, z u is the displacement component along the loading direction, $f(r)$ is the surface profile of the indenter tip, h is the displacement of the indenter, and a is the radius of the contact between the indenter and the SMA. The far-field condition requires, $\sigma_{rz}$(r, z) $\rightarrow$ 0, $\sigma_{zz}$(r, z) $\rightarrow$ 0, $u_r$ (r, z) $\rightarrow$ 0, and $u_z$ (r, z) $\rightarrow$ 0 as r $\rightarrow \infty$ or z $\rightarrow$ -$\infty$. The indentation load applied to the indenter can be calculated as

$$F = -2\pi \int_0^a \sigma_{zz}(r,0) r dr \tag{2}$$

## 2.2 Material model for SMAs

In the present study, the SMAs are assumed to exhibit superelastic-plastic behavior, as sketched by the idealized stress-strain curve shown in Figure 2 [38]. $\sigma_L^S$ and $\sigma_L^E$ are the start and end stresses for the forward transformation, respectively; $\sigma_U^S$ and $\sigma_U^E$ are the start and end stresses for the reverse transformation, respectively; $E_a$ and $E_m$ are the elastic modulus of the austenite and the martensite, respectively; $\varepsilon_L$ is the transformation strain.

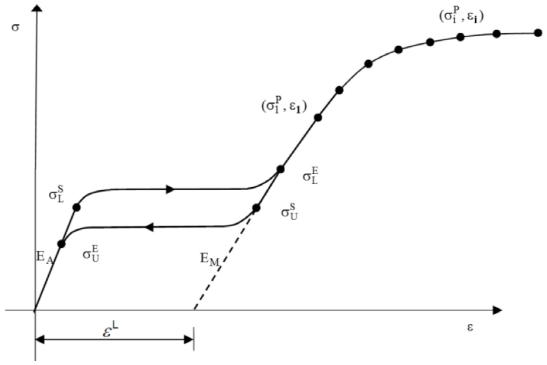


**Figure 2** Sketch of the idealized stress-strain curve for the SMAs

The plastic behavior of the SMAs was described by the power law work-hardening model [39]:

$$\sigma = \sigma_1^P \left( E\varepsilon / \sigma_1^P \right)^n \tag{3}$$

where E is the elastic modulus, $\sigma_l^p$ is the stress at the onset of plastic deformation, n is the work hardening exponent. In the present study, n varied from 0.1-0.5. Two materials were selected for studying the indentation behavior of the SMAs: a binary NiTi SMA and a ternary NiTiHf SMA. The present NiTi ($Ni_{55.9}Ti_{44.1}$) and NiTiHf ($Ni_{50.3}Ti_{29.7}Hf_{20}$) have reference temperatures of 296 K [29] and 517 K [31], respectively. One distinct characteristic between these two SMAs is the elastic modulus: for NiTi, the austenite phase has a greater modulus than the martensite ($E_a > E_m$); for NiTiHf, the austenite phase has a smaller modulus than the martensite ($E_a < E_m$). Table 1 summarizes the detailed properties of these two SMAs, which were used as inputs in ABAQUS.

**Table 1** Summary of material properties for the two SMAs

| Properties | NiTi [29] | NiTiHf [31] |
|---|---|---|
| Austenitic Young's Modulus, $E_a$ | 40800 MPa | 48767 MPa |
| Martensitic Young's Modulus, $E_a$ | 24200 MPa | 69636 Mpa |
| Austenite Poisson's Ratio, $v_a$ | 0.3 | 0.3 |
| Martensite Poisson's Ratio, $v_m$ | 0.3 | 0.3 |
| Transformation Strain, $\varepsilon_L$ | 0.0447 | 0.0285 |
| Austenitic Start Stress, $\sigma_L^S$ | 390 Mpa | 374 Mpa |
| Austenitic Finish Stress, $\sigma_L^E$ | 479 MPa | 211 Mpa |
| Martensitic Start Stress, $\sigma_U^S$ | 106 MPa | 535 Mpa |
| Martensitic Finish Stress, $\sigma_U^E$ | 50 MPa | 645 Mpa |
| Reference Temperature, $T_0$ (Austenitic end temperature) | 296 K | 517 K |
| Plastic Yield Strength, $\sigma_1^P$ | 643 MPa | 816 MPa |

# 3 Results and discussion

## 3.1 Indentation loading-unloading responses of SMAs

Figure 3 shows the progressive indentation loading-unloading curves for NiTi and NiTiHf SMAs with a strain hardening index of 0.5. The indentation results have been normalized by using the parameters of $F/\pi R^2$ and $h/R$ for the indentation load and the indentation depth, respectively.

As shown in Figure 3(a) and Figure 3(c), at low indentation depths (h/R¡0.1%), the deformations under the indenter are purely elastic, and the loading curves follow the classic Hertz theory [31]:

$$F = \frac{4E}{3(1-v)^2} R^{1/2} h^{3/2} \tag{4}$$

where E is the elastic modulus of the material at the initial state (which is the austenite phase for both SMAs). The agreements between FEM and Hertz's analytical solutions also serve as validations for the finite element model (element sizes, boundary conditions, etc.). As the load increases, the indentation loading curves begin to deviate from the Hertz predictions, indicating that phase transformation and/or plastic deformation have occurred in the SMAs beneath the indenter.

At small indentation forces, the indentation loading-unloading curves are seen to form closed loops for both SMAs (Figure 3), indicating that the SMAs have recovered to their original positions after the withdrawal of the indenter and that the deformation in the SMAs is predominately superelastic. However, as the indentation load increases, the loadingunloading curves exhibit residual indentations, indicating that permanent plastic deformation occurred after unloading the indent.

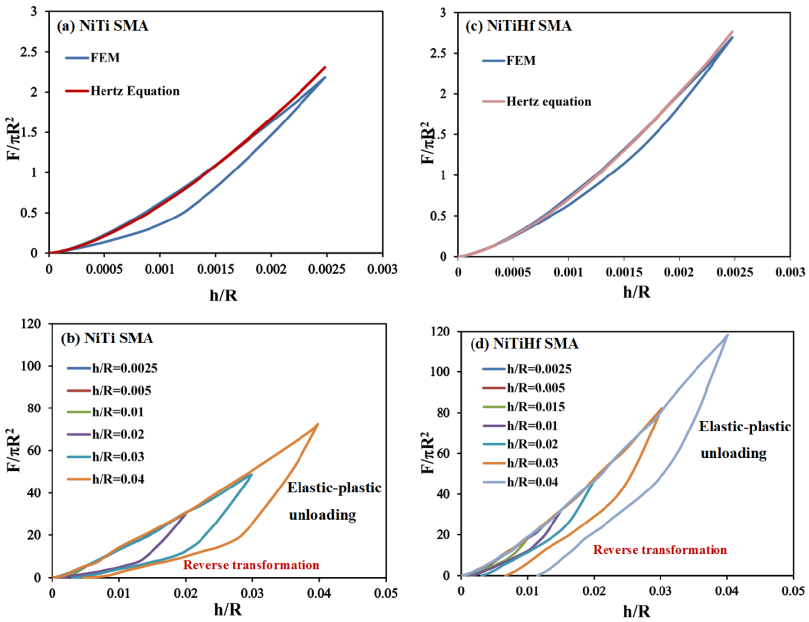


**Figure 3** The indentation loading-unloading curves for (a, b) NiTi (left figures), and (c, d) NiTiHf (right figures) with n=0.5: Top row: validations for the finite element model by comparing the FEM and Hertz's analytical solutions at small indentation depth, and Bottom row: FEM results at larger indentation depth.

It is noted that the indentation unloading responses of the SMAs show distinct differences from those of conventional materials. For conventional single-phase materials, the indentation unloading curves are continuous and well approximated by a power law function [1]. In contrast, the unloading curves for the SMAs are clearly bifunctional (Figure 3(b) and Figure 3(d)). The initial portion of the unloading curve is a response to typical elastic or elastic-plastic deformation and can be approximated by the power law function. The second portion of the unloading curve, as indicated by a sharp change in slope, is a result of reverse phase transformation (martensite→austenite) due to the change in indentation load. By curve-fitting the initial portions of unloading curves shown in Figure 3, the elastic contact stiffness can be obtained for the SMAs [1]:

$$S = \left(\frac{\partial F}{\partial h}\right)_h = h_{max} \tag{5}$$

Following Joslin and Oliver [26], the normalized contact stiffness, the ratio of load to the square of stiffness ($F/S^2$), is calculated

$$\frac{F}{S^2} = \frac{\pi}{(2\beta)^2}\frac{H}{E^2} \tag{6}$$

where $\beta$ is a geometric constant depending upon the profile of the indenter tip. For spherical indenter, $\beta$ = 0.75. H and E are the hardness and modulus of the testing material, respectively.

This normalized contact stiffness ($F/S^2$) has been known as an essential parameter in the analysis of the indentation experiment [1,40]. As shown in Equation 6, $F/S^2$ is constant since it is dependent only on the material properties (E, H) and independent of the indentation depth and contact area. Further, it does not depend on the pile-up or sink-in behavior and thus is irrelevant to the deformation that occurred in the materials. Due to these unique characteristics, $F/S^2$ has been deemed to be a valuable quantity in calibrating the nanoindentation experiments (both physical and numerical experiments). The normalized contact stiffness ($F/S^2$) for both SMAs is calculated and shown in Figure 4. The contact stiffness is not constant; rather, they increase with the indentation depth. This phenomenon confirms that the indentation response of the shape memory alloys is drastically different from that of conventional materials. For the phase transformable materials, the microstructure and, thus, the material properties (E and H) change continuously as the load changes during the indentation.

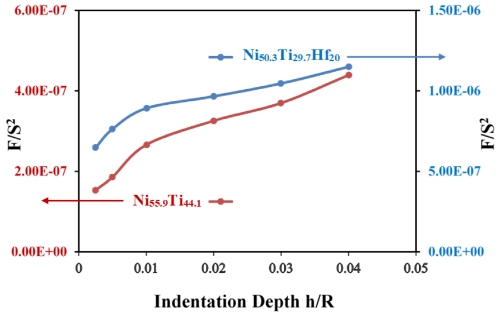


**Figure 4** Variations of the normalized contact stiffness as a function of indentation depth for SMAs

## 3.2 Load-induced phase transformation during indentation

The phase transformation in the SMA specimen during the indentation process can be simulated quantitatively using the finite element method [38]. Figure 5 shows the evaluations of austenite and martensite phases in the SMAs under a spherical indenter for NiTi and NiTiHf at the left and right of the figure, respectively. The volume fraction of martensite phase ($\theta_m$) has been implemented as a user-defined output in ABAQUS through the material user subroutine [38]. The value of $\theta_m$ is calculated at every integration point of each element for every load step, whose magnitude ranges from 0 to 1. When $\theta_m$ = 0, the material is entirely austenite, and when $\theta_m$ = 1 the material is fully martensite. At the initial stage of the indentation, where the load is small, the material is fully austenite ($\theta_m$ = 0, Figure 5(a) and Figure 5(b)). As the load increases, the austenite starts to transform partially into martensite. The transformation begins right beneath the indenter face, where the stress is at its highest [39, 41, 42]. Upon continuous loading, a fully transformed martensite zone (labeled as "M" in the figures) is developed and expanded ($\theta_m$ = 1), which is in the form of a hemispherical disk. The fully transformed martensite zone is enclosed by a martensiteaustenite transition zone where $0 < \theta_m < 1$. Outside this transition zone is the austenite phase ($\theta_m$ = 0) since there is no acting load in the material in the far field (Figure 5).

By manually selecting all "transformed" elements, the "average" volume fraction of the martensite phase ($\bar{\theta}_m$) in the SMA may be calculated. Figure 6 show the variations of the averaged volume fraction of martensite of the SMA specimen as a function of indentation depth (load) for NiTi and NiTiHf, respectively. It is observed that there is no presence of martensite ($\bar{\theta}_m$ = 0) at small depths since the material is in a complete austenite phase. As the load increases, the transformation begins, and the fraction of the martensite phase ($\bar{\theta}_m$) starts to increase. However, the rate of increase in $\bar{\theta}_m$ decreases with the increase of indentation depth (h). The overall response of the volume fraction of martensite follows a power law relation.

According to the idealized stress-strain response of an SMA under uniaxial loading (Figure 2), the austenite phase ($\bar{\theta}_m$ = 0) starts transforming partially into the martensite phase and eventually becomes full martensite ($\bar{\theta}_m$ = 1) under sufficient load ($\sigma > \sigma_U^S$). However, such an ideal transformation may not occur during the indentation loading since the indentation is

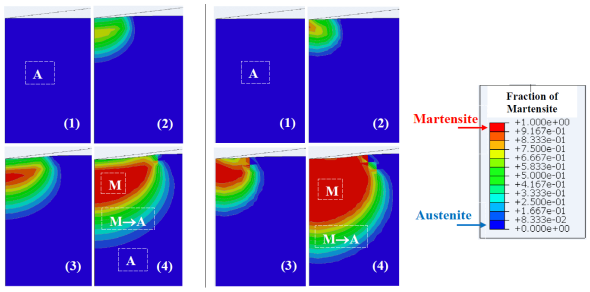


**Figure 5** Contours showing the phase transformation of (a) $Ni_{55.9}Ti_{44.1}$ (Left) and (b) $Ni_{50.3}Ti_{29.7}Hf_{20}$ (Right) SMAs under the loading of a spherical indenter. M: martensite zone, M→A: martensite-austenite transition zone, A: austenite zone.

a localized mechanical test. During the indentation, it is known that the specimen is highly stressed right beneath the indenter face and is stress-free at regions far away from the indenter. Between these two regions is the transition zone, where the stress diminishes gradually. Due to this stress gradient, the load from a pointed indenter can only induce a localized phase transformation, *i.e.*, the transformation of the martensite phase under the indentation load will be gradient. Therefore, the magnitude of $\bar{\theta}_m$ in an indentation specimen might never reach to the unity (Figure 6).

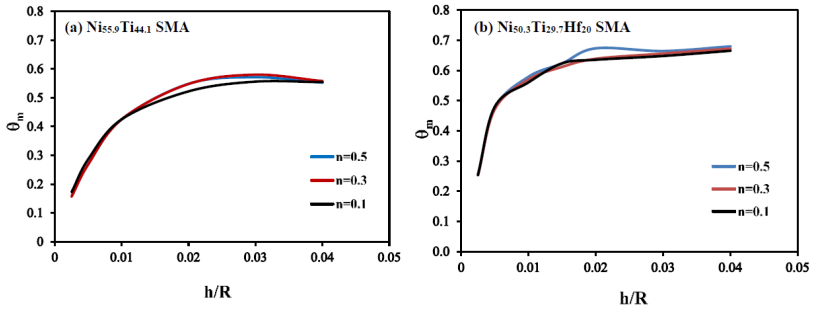


**Figure 6** Variation of average volume fraction of martensite phase in (a) NiTi and (b) NiTiHf as a function of indentation depth

## 3.3 Indentation modulus of SMAs

Based on the contact stiffness (S) computed from Equation 5, two important contact parameters between the indenter and the solid, the actual contact depth ($h_c$) and the contact area ($A_c$) can be calculated [1]:

$$h_c = h - \beta\frac{F}{S} \tag{7a}$$

$$A_c = \pi\left(2h_cR - h_c^2\right) \tag{7b}$$

Following the standard Oliver-Pharr method [1], the reduced modulus ($E_r$) is calculated, which is subsequently used to compute the modulus (E) of the SMA that is in contact with the indenter by using:

$$E_r = \frac{\sqrt{\pi}}{2\beta}\frac{S}{\sqrt{A_c}} \tag{8a}$$

$$E = \frac{1-v^2}{\frac{1}{E_r} - \frac{1-v_i^2}{E_i}} \tag{8b}$$

where $E_i$ and $v_i$ are the elastic modulus and Poisson's ratio of the diamond indenter ($E_i$ = 1140 GPa and $v_i$ = 0.07).

Figure 7 shows the variation of elastic modulus (E) of the SMA as a function of indentation depth for NiTi and NiTiHf. The modulus would remain constant for conventional single-phase materials regardless of the indentation depth (load) [1]. It is clear that the modulus of SMAs changes continuously with the indentation depth (load). An SMA may be considered a composite consisting of austenite and martensite phases. Thus, the overall modulus of the composite may be estimated once the volume fractions of the two constituents are known. As the load increases, the fraction of the martensite phase ($\bar{\theta}_m$) in the material increases and the fraction of austenite phase ($\bar{\theta}_a$) in the material decreases. For NiTi SMA where $E_m$ is lower than $E_a$, the total modulus of the composite is seen to decrease with the depth; for NiTiHf SMA where $E_m$ is greater than $E_a$, the total modulus of the composite is seen to increase with the depth.

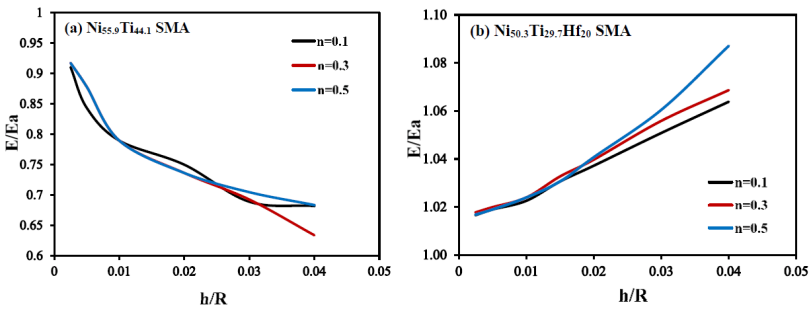


**Figure 7** Variation of indentation modulus as a function of indentation depth for (a) NiTi and (b) NiTiHf SMAs

The indentation test also allows for direct prediction of the modulus of the austenite phase, $E_a$. As shown in Figure 3, the SMAs are predominately elastic under low loads and the loading curves follow the Hertz theory. Therefore, rearranging Equation 4 would directly yield the modulus of the austenite phase ($E_a$ = E). Figure 8 displays the values of $E_a$ calculated from Equation 4 by using the initial portions of the load-depth curves obtained at various indentation loads. It is seen that the predictions are in excellent agreement with the input values obtained from the uniaxial test (Table 1).

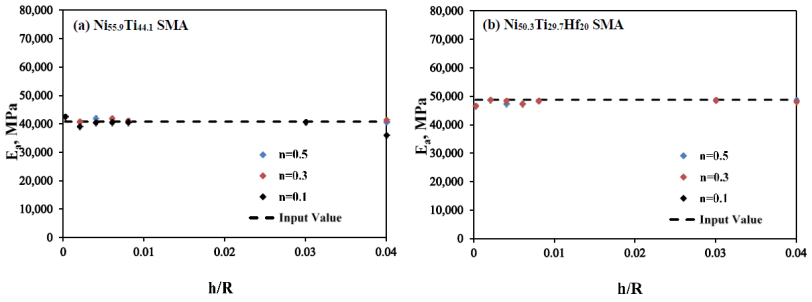


**Figure 8** The elastic modulus prediction for the austenite phase in (a) NiTi and (b) NiTiHf SMAs computed directly from indentation load-depth curves obtained at various indentation loads

However, estimating the modulus of the martensite phase ($E_m$) from the indentation test may not be straightforward. A methodology has been suggested to compute Em by assuming the Kelvin arrangement of the two constituent phases in the SMA: $\frac{1}{E} = \frac{\bar{\theta}_a}{E_a} + \frac{\bar{\theta}_m}{E_m}$ [29]. This method has been tried in the present study, but the results show that the percentage of discrepancy in $E_m$ is rather significant, as high as over 40%. The primary reason for such significant errors is due to the stress gradient under the indenter. Unlike conventional uniaxial tests, indentation is a localized test; thus, the stress (load) beneath the indenter face is not uniform. As a result, the phase transformation beneath the indenter face shows a gradient, as shown in Figure 5. Therefore, the fractions of each phase, martensite phase $\bar{\theta}_m$ and austenite phase $\bar{\theta}_a$, are simply the volumetric average of each material at a finite region under the indenter. There will never be a complete transformation of martensite phase under the indentation load and thus, the rules of the mixture-based Kelvin model may not be valid for estimating the properties of two-phase SMA under the indentation test. Furthermore, it should also be noted that the modulus of martensite depends on whether it forms self-accommodating or reoriented (detwinned) structures.

# 4 Conclusion

The present study uses the finite element method to comprehensively examine the indentation load-induced mechanical behaviors of NiTi and NiTiHf shape memory alloys. The phase transformations are clearly evidenced in the indentation load-depth responses of the SMAs. It is observed that the unloading curves of the SMAs show sharp slope changes as the reverse transformations (martensite→austenite) begin. The phase transformation phenomena induced by the indentation load are found to be different from that induced by a uniaxial load on a tensile/compression specimen. Since the load under an indenter shows a gradient, the phase transformation in SMA beneath the indenter face can not be fully completed. The evaluation of the average volume fraction of martensite induced by indentation load generally follows a power-law function. The overall modulus of the SMAs obtained from the indentation test varies

continuously with the indentation depth (load). For NiTi, the modulus decreases with the depth due to a lower modulus of martensite phase. In contrast, for NiTiHf, the modulus increases with the depth due to a higher modulus of martensite phase. The predicted young modulus during indentation simulation agrees well with experimental results. Lastly, the phase transformation process under a spherical indenter has not been significantly affected by the plastic properties of the SMAs.

# References


[1] Oliver WC and Pharr GM. An improved technique for determining hardness and elastic modulus using load and displacement sensing indentation experiments. Journal of materials research, 1992, **7**(6): 1564-1583.
https://doi.org/10.1557/JMR.1992.1564

[2] Doerner MF and Nix WD. A method for interpreting the data from depth-sensing indentation instruments. Journal of Materials Research, 1986, **1**(4): 601-609.
https://doi.org/10.1557/JMR.1986.0601

[3] Mayo MJ, Siegel RW, Liao YX, *et al*. Nanoindentation of nanocrystalline ZnO. Journal of Materials Research, 1992, **7**: 973-979.
https://doi.org/10.1557/JMR.1992.0973

[4] Cheng L, Xia X, Yu W, *et al*. Flat-punch indentation of viscoelastic material. Journal of Polymer Science Part B: Polymer Physics, 2000, **38**(1): 10-22.
https://doi.org/10.1002/(SICI)1099-0488(20000101)38:1⟨10::AID-POLB2⟩3.0.CO;2-6

[5] Lu YC and Shinozaki DM. Characterization and modeling of large displacement micro-/nano-indentation of polymeric solids. Journal of Engineering Materials and Technology, 2008, **130**(4): 041001.
https://doi.org/10.1115/1.2969250

[6] Pharr GM, Harding DS and Oliver WC. Measurement of fracture toughness in thin films and small volumes using nanoindentation methods. Mechanical properties and deformation behavior of materials having ultra-fine microstructures. NATO ASI Series, 1993, **233**: 449-461.
https://doi.org/10.1007/978-94-011-1765-4_29

[7] Volinsky AA, Moody NR and Gerberich WW. Nanoindentation of Au and Pt/Cu thin films at elevated temperatures. Journal of Materials Research, 2004, **19**(9): 2650-2657.
https://doi.org/10.1557/JMR.2004.0331

[8] Zhang Q, Lu YC, Du F, *et al*. Viscoelastic creep of vertically aligned carbon nanotubes. Journal of physics D: Applied physics, 2010, **43**(31): 315401.
https://doi.org/10.1088/0022-3727/43/31/315401

[9] Fulcher JT, Lu YC, Tandon GP, *et al*. Thermomechanical characterization of shape memory polymers using high temperature nanoindentation. Polymer Testing, 2010, **29**(5): 544-552.
https://doi.org/10.1016/j.polymertesting.2010.02.001

[10] Bansiddhi A, Sargeant TD, Stupp SI, *et al*. Porous NiTi for bone implants: a review. Acta biomaterialia, 2008, **4**(4): 773-782.
https://doi.org/10.1016/j.actbio.2008.02.009

[11] Elahinia MH, Hashemi M, Tabesh M, *et al*. Manufacturing and processing of NiTi implants: A review. Progress in materials science, 2012, **57**(5): 911-946.
https://doi.org/10.1016/j.pmatsci.2011.11.001

[12] Jani JM, Leary M, Subic A, *et al*. A review of shape memory alloy research, applications and opportunities. Materials & Design (1980-2015), 2014, **56**: 1078-1113.
https://doi.org/10.1016/j.matdes.2013.11.084

[13] Saedi S, Saghaian SE, Jahadakbar A, *et al*. Shape memory response of porous NiTi shape memory alloys fabricated by selective laser melting. Journal of Materials Science: Materials in Medicine, 2018, **29**: 1-12.
https://doi.org/10.1007/s10856-018-6044-6

[14] Saghaian SE, Nematollahi M, Toker G, *et al*. Effect of hatch spacing and laser power on microstructure, texture, and thermomechanical properties of laser powder bed fusion (L-PBF) additively manufactured NiTi. Optics & Laser Technology, 2022, **149**: 107680.
https://doi.org/10.1016/j.optlastec.2021.107680

[15] Moghaddam NS, Saedi S, Amerinatanzi A, *et al*. Influence of SLM on compressive response of NiTi scaffolds. Behavior and Mechanics of Multifunctional Materials and Composites XII. SPIE, 2018, **10596**: 60-66.

[16] Frâemond M and Miyazaki S. Shape Memory Alloys. Springer, New York, 1996.
https://doi.org/10.1007/978-3-7091-4348-3

[17] Otsuka K. and Wayman CM. Shape memory materials. Cambridge university press, 1999.

[18] Fu Y, Du H, Huang W, *et al*. TiNi-based thin films in MEMS applications: a review. Sensors and Actuators A: Physical, 2004, **112**(2-3): 395-408.
https://doi.org/10.1016/j.sna.2004.02.019

[19] Zhang L, Xie C and Wu J. Progress in research on shape memory alloy films in MEMS field. Materials Review, 2006, **2**: 109-113.

[20] Saedi S, Saghaian SE, Jahadakbar A, *et al*. Shape memory response of porous NiTi shape memory alloys fabricated by selective laser melting. Journal of Materials Science: Materials in Medicine, 2018, **29**: 1-12.
https://doi.org/10.1007/s10856-018-6044-6
[21] Saghaian SE, Amerinatanzi A, Moghaddam NS, *et al*. Mechanical and shape memory properties of triply periodic minimal surface (TPMS) NiTi structures fabricated by selective laser melting. Biol Eng Med, 2018, **3**: 1-7.
https://doi.org/10.15761/BEM.1000152
[22] Moghaddam NS, Saedi S, Amerinatanzi A, *et al*. Influence of SLM on compressive response of NiTi scaffolds. Behavior and Mechanics of Multifunctional Materials and Composites XII. SPIE, 2018, **10596**: 60-66.
[23] Gall K, Juntunen K, Maier HJ, *et al*. Instrumented micro-indentation of NiTi shape-memory alloys. Acta Materialia, 2001, **49**(16): 3205-3217.
https://doi.org/10.1016/S1359-6454(01)00223-3
[24] Liu R, Li DY, Xie YS, *et al*. Indentation behavior of pseudoelastic TiNi alloy. Scripta Materialia, 1999, **41**(7): 691-696.
https://doi.org/10.1016/S1359-6462(99)00199-2
[25] Ni W, Cheng YT and Grummon DS. Recovery of microindents in a nickel–titanium shape-memory alloy: a "self-healing" effect. Applied Physics Letters, 2002, **80**(18): 3310-3312.
https://doi.org/10.1063/1.1476064
[26] Ni W, Cheng YT and Grummon DS. Microscopic superelastic behavior of a nickel-titanium alloy under complex loading conditions. Applied Physics Letters, 2003, **82**(17): 2811-2813.
https://doi.org/10.1063/1.1569984
[27] Amini A, Yan W and Sun Q. Depth dependency of indentation hardness during solid-state phase transition of shape memory alloys. Applied Physics Letters, 2011, **99**(2): 021901.
https://doi.org/10.1063/1.3603933
[28] Kang G and Yan W. Scaling relationships in sharp conical indentation of shape memory alloys. Philosophical Magazine, 2010, **90**(5): 599-616.
https://doi.org/10.1080/14786430903213346
[29] Kan Q, Yan W, Kang G, *et al*. Oliver–Pharr indentation method in determining elastic moduli of shape memory alloys—a phase transformable material. Journal of the Mechanics and Physics of Solids, 2013, **61**(10): 2015-2033.
https://doi.org/10.1016/j.jmps.2013.05.007
[30] Tabor D. The hardness of metals. Oxford university press, 2000.
[31] Karaca HE, Saghaian SM, Ded G, *et al*. Effects of nanoprecipitation on the shape memory and material properties of an Ni-rich NiTiHf high temperature shape memory alloy. Acta Materialia, 2013, **61**(19): 7422-7431.
https://doi.org/10.1016/j.actamat.2013.08.048
[32] Andani MT, Moghaddam NS, Haberland C, *et al*. Metals for bone implants. Part 1. Powder metallurgy and implant rendering. Acta biomaterialia, 2014, **10**(10): 4058-4070.
https://doi.org/10.1016/j.actbio.2014.06.025
[33] Pattanayak DK, Fukuda A, Matsushita T, *et al*. Bioactive Ti metal analogous to human cancellous bone: Fabrication by selective laser melting and chemical treatments. Acta Biomaterialia, 2011, **7**(3): 1398-1406.
https://doi.org/10.1016/j.actbio.2010.09.034
[34] Yan C, Hao L, Hussein A, *et al*. Ti–6Al–4V triply periodic minimal surface structures for bone implants fabricated via selective laser melting. Journal of the mechanical behavior of biomedical materials, 2015, **51**: 61-73.
https://doi.org/10.1016/j.jmbbm.2015.06.024
[35] Lindner M, Hoeges S, Meiners W, *et al*. Manufacturing of individual biodegradable bone substitute implants using selective laser melting technique. Journal of Biomedical Materials Research Part A, 2011, **97**(4): 466-471.
https://doi.org/10.1002/jbm.a.33058
[36] Saghaian SM, Karaca HE, Tobe H, *et al*. High strength NiTiHf shape memory alloys with tailorable properties. Acta Materialia, 2017, **134**: 211-220.
https://doi.org/10.1016/j.actamat.2017.05.065
[37] Nematollahi M, Toker G, Saghaian SE, *et al*. Additive manufacturing of ni-rich nitihf 20: Manufacturability, composition, density, and transformation behavior. Shape Memory and Superelasticity, 2019, **5**: 113-124.
https://doi.org/10.1007/s40830-019-00214-9
[38] Bae JW, Jung J, Kim JG, *et al*. On the phase transformation and dynamic stress–strain partitioning of ferrous medium-entropy alloy using experimentation and finite element method. Materialia, 2020, **9**: 100619.
https://doi.org/10.1016/j.mtla.2020.100619
[39] Johnson KL and Johnson KL. Contact mechanics. Cambridge University Press, 1987.
[40] Joslin DL and Oliver WC. A new method for analyzing data from continuous depth-sensing microindentation tests. Journal of Materials Research, 1990, **5**: 123-126.
https://doi.org/10.1557/JMR.1990.0123
[41] Biwa S and Storåkers B. An analysis of fully plastic Brinell indentation. Journal of the Mechanics and Physics of Solids, 1995, **43**(8): 1303-1333.
https://doi.org/10.1016/0022-5096(95)00031-D
[42] Sneddon IN. The relation between load and penetration in the axisymmetric Boussinesq problem for a punch of arbitrary profile. International Journal of Engineering Science, 1965, **3**(1): 47-57.